



In situ synthesized S-type heterojunction $\text{Bi}_2\text{O}_2\text{CO}_3/\text{CuBi}_2\text{O}_4$ enable efficient NIR light-driven H_2O_2 activation for water purification

Jinyong Qu^{a,1}, Dongpeng Zhang^{a,1}, Yanxiao Li^a, Pengfei Wang^a, Yueshuang Mao^a,
Tao Zhang^a, Sihui Zhan^{a,*}, Yi Li^{b,*}

^a MOE Key Laboratory of Pollution Processes and Environmental Criteria Tianjin Key Laboratory of Environmental Remediation and Pollution Control College of Environmental Science and Engineering Nankai University, Tianjin 300350 PR China

^b Tianjin Key Laboratory of Molecular Optoelectronic Sciences Department of Chemistry, School of Science & Collaborative Innovation Center of Chemical Science and Engineering (Tianjin) Tianjin University, Tianjin 300072 PR China

ARTICLE INFO

Keywords:

Fenton-like
Near-infrared light
S-scheme charge transfer
Wastewater treatment
Organic pollutant

ABSTRACT

Hydrogen peroxide (H_2O_2) was the most commonly used oxidant in advanced oxidation processes to degrade emerging organic pollutants. However, photoactivation of H_2O_2 by catalysts had the problems of narrow pH application range and low solar energy utilization rate. Herein, the $\text{Bi}_2\text{O}_2\text{CO}_3/\text{CuBi}_2\text{O}_4$ heterojunction photocatalyst was *in-situ* synthesized, which could activate H_2O_2 under NIR radiation to degrade organic pollutants and complex heavy metal pollutants. Both *in-situ* irradiation XPS spectra and DFT supported the S-type charge transfer mechanism. Driven by the IEF and bending band, photogenerated electrons were transferred from $\text{Bi}_2\text{O}_2\text{CO}_3$ to CuBi_2O_4 , which inhibited the recombination of carriers and promoted the activation of H_2O_2 . The activation rate constant of CBO-2/Vis/ H_2O_2 system for H_2O_2 was 0.0403 min^{-1} , which was 36.6 times that of the original BOC. This work provided new systematic insights into H_2O_2 activation by S-scheme heterojunction and had implications for wastewater treatment.

1. Introduction

The pollution of the aquatic environment caused by organic pollutants, heavy metal pollutants, and the formation of complex heavy metal pollutants due to their toxicity and resistance to degradation, had been attracting more and more attention from the public [1–3]. Such as in recent years, with the spread of global health problems, the use of acetaminophen (APAP) tablets had increased dramatically, posing a threat to the environment and health. Advanced oxidation processes (AOPs), such as Fenton-like oxidation, ozone oxidation, chlorine oxidation, and electrochemical oxidation, were promising methods for the removal of organic pollutants and heavy metal complex pollutants due to their high efficiency in producing oxidizing free radicals under environmental conditions [4–8]. Hydrogen peroxide (H_2O_2) was eco-friendly operation and cost-effective nature [9]. The Fenton-like using H_2O_2 as the oxidant has attracted much attention due to its high efficiency in the conversion of refractory organics. However, the low activation efficiency and high usage of H_2O_2 still face challenges in practical applications. Photo-Fenton had been more widely used for the

degradation of various organic pollutants due to its low cost, ease of operation, mild reaction conditions, and high efficiency [8,10]. But there were still some challenges in the application of the traditional photo-Fenton reaction, such as the relatively low conversion efficiency of $\text{Fe}^{3+}/\text{Fe}^{2+}$ due to low concentration of photogenerated electrons, this limited the activation of H_2O_2 etc. [11–13].

At present, studies on the photo-Fenton reaction could be broadly classified into two categories. Firstly, hydroxyl radical ($\bullet\text{OH}$) could be generated by using H_2O_2 and iron salt as reagents [14,15]. Meanwhile, Fe^{3+} might be reduced by H_2O_2 , which promoted an oxidation reaction. Secondly, the active electrons generated by the photoexcited catalyst directly or indirectly helped to activate H_2O_2 and produce ROS [16,17]. For example, the introduction of ligand cluster charge transfer excitation into the photo-Fenton process accelerated the conversion of $\text{Fe}^{3+}/\text{Fe}^{2+}$ and greatly improved the ability to deoxidize pollutants by visible light irradiation at neutral pH [18]. And, in order to lower the activation barrier of H_2O_2 under visible light irradiation and increase the production efficiency of $\bullet\text{OH}$, the local coordination structure and electron density of the catalyst might be increased by modifying the surface

* Corresponding authors.

E-mail addresses: sihuizhan@nankai.edu.cn (S. Zhan), liyi@tju.edu.cn (Y. Li).

¹ These authors contributed equally to this work.

relaxation of the catalyst [19]. Besides, the iron monoatomic photocatalyst could direct electrons through defect engineering, and the formation of high electron density remarkably improved the conversion efficiency of H_2O_2 under visible light irradiation [20]. This reaction process still had shortcomings that limited its practical application, such as low production of photogenerated electrons, poor transfer efficiency, and low utilization rate of sunlight.

In general, it proved to be an effective means to increase the photon utilization efficiency by extending the photo-response range of the catalyst [21]. Since near-infrared light was thought to be able to be effectively absorbed by narrow-band photocatalysts, this increased the efficiency of solar energy utilization [22,23]. But the redox capacity of narrow-band photocatalysts was inevitably reduced [24,25]. To solve these problems, it remained a great challenge to find extremely efficient activated H_2O_2 photocatalysts with higher solar energy utilization efficiency that could be extended to the near-infrared (NIR) range. The S-type heterojunction system had strong redox ability due to its unique electron transfer pathway, which could effectively suppress the interface recombination of photoexcited charge carriers [8,26,27]. In recent years, it has received increasing attention. For example, by removing the suspension bond of the heterogeneous interface, the height of the carrier transport barrier was reduced, the electronic structure of the interface was optimized, charge separation was promoted and photocatalytic activity was enhanced [28]. In addition, a large number of oxygen vacancies were generated on the catalyst, resulting in electron delocalization effect. This increased the conductivity and triggered the local production of O_2 in the redox cycle to activate H_2O_2 [29]. However, the heterojunctions reported to date were affected by poor interfacial bonding and/or the complexity of synthesis schemes, so most heterojunctions had high interfacial transfer resistance. Previous studies had shown that the *in-situ* strategy could achieve a uniform distribution of one component on the other with a tight interface, which was conducive to carrier transport and separation [30–32]. Inspired by this, it would be very interesting and meaningful to construct *in-situ* heterojunction to activate H_2O_2 under near-infrared light.

In conclusion, the *in-situ* synthesized $\text{Bi}_2\text{O}_2\text{CO}_3/\text{CuBi}_2\text{O}_4$ (BOC/CBO, abbreviated as CBO-x) heterojunction model system showed excellent photocatalytic degradation of organic pollutants and complex heavy metal pollutants. The photocatalytic degradation rate constants of CBO-2 for APAP were 3.6 times and 36.6 times that of CBO and BOC, respectively. Under NIR irradiation, the photocatalytic degradation rate constants of CBO-2 for APAP were 2.3 times and 21.2 times that of CBO and BOC, respectively. According to ISI-XPS and DFT calculations, an S-type electron transfer path was formed between CBO and BOC. Driven by the interface IEF and bending band, the photogenerated electrons in CB of BOC spontaneously slide towards VB of CBO, which effectively enhanced the charge separation and transfer process. This special electron transfer path increased the number of electrons transferred from the photocatalyst to H_2O_2 , confirming that the construction of heterojunctions could enhance the photocatalytic activity of H_2O_2 . This work provided new ideas for *in-situ* synthesis of S-type heterojunctions and further insights into charge migration during photocatalytic activation of H_2O_2 to treat pollutants.

2. Experimental section

2.1. Preparation of catalysts

CuBi_2O_4 nanorods were prepared by a one-step hydrothermal method and $\text{Bi}_2\text{O}_2\text{CO}_3/\text{CuBi}_2\text{O}_4$ heterojunction composites were synthesized by *in-situ* synthesis [33]. The details for preparing the catalysts were displayed in Supporting information (Section S1). According to the quality of polyvinyl pyrrolidone (PVP) added to CuBi_2O_4 , the prepared composites were named CBO, CBO-1, CBO-2, and CBO-3, respectively.

2.2. Characterization

The microstructures of the prepared catalyst were observed by using a Hitachi SU8010 scanning electron microscope (SEM) and a JEOL JEM-2100 F transmission electron microscope (TEM). The Autosorb-IQ Automated Gas Sorption Analyzer (Quantachrome) was used to record the N_2 adsorption-desorption isotherms. To determine the purity and crystallinity of the photocatalysts, powder X-ray diffraction (XRD) was performed using Cu K radiation ($\lambda = 0.15418 \text{ nm}$) on a Rigaku D/Max 2200PCX-ray diffractometer. Thermo Nicolet IS5 fourier transform infrared spectra (FTIR) spectrometer equipped with a liquid nitrogen-cooled MCT detector was employed to measure the FTIR spectra of the photocatalysts. Thermal ESCALAB 250 electron spectrometer performed X-ray photoelectron spectroscopy (XPS) to ascertain the components elements and chemical states of the materials. The binding energies were calibrated using C 1s peak at 284.8 eV. And *in-situ* irradiated X-ray photoelectron spectroscopy (ISI-XPS) was carried out on an electron spectrometer (ESCALAB 210, VG, UK) to research the electron density changes on photocatalysts under light irradiation. Raman spectra of samples were tested by Confocal Raman spectrometer (TEO SR-500I-A, Hong Kong, China). An electron spin resonance (ESR) spectrometer was used to record the reactive species (JES-FA200, Bruker). The UV/Vis-NIR diffuse reflectance spectra of the produced samples was attained using a UV-Vis spectrophotometer (Shimadzu). Photoluminescence spectra (PL) were captured using a 325 nm excitation wavelength and an Edinburgh Instruments FL S920 P spectrophotometer. Agilent 6110 quadrupole mass spectrometry was used to detect contents of photo-degradation intermediates in positive mode. The intermediates of degraded APAP were identified using high-resolution mass spectrometry (UPLC-HRMS, Orbitrap Fusion, Thermo, USA). 20 μL of the extract was injected automatically into the UPLC-HRMS system with a Waters C18 column (250 mm \times 4.6 mm, 5 μm). The eluent was methanol and water, and the flow rate was 1 mL min^{-1} . The LC/MS operated in the negative ionization (NI) mode with a dwell time of 200 ms and a scan range of 50–500 Da. All photoelectrochemical measurements were performed by using a CHI660E electrochemical analyzer (CHI Shanghai, Inc.). The removal rate of total organic carbon (TOC) was conducted on a TOC-V CPH (multi N/C3100).

2.3. Photocatalytic degradation experiments

The photocatalytic performance of the synthesized photocatalyst was assessed by the degrading impact of the pollutant in visible light ($\lambda > 420 \text{ nm}$ /420 nm $< \lambda < 800 \text{ nm}$) and near-infrared light ($\lambda > 800 \text{ nm}$). The light source was a 300 W Xenon lamp using CEL-HXF300, which had an 800 nm, 420–800 nm or 420 nm optical filter. First of all, the composite material (40 mg) was dispersed into 50 mL (20 ppm APAP, 20 ppm Cu-EDTA) solution with 10 mg/L concentration. In the dark, stir the suspension so that it reaches adsorption and desorption equilibrium for 15 min. After that, 30 microliters (30%) of H_2O_2 were added during the photocatalytic reaction and 2 mL samples were taken every 15 min. Secondly, the degradation rate of APAP was assessed by the absorbance change shown by a UV-Visible spectrophotometer at the absorption wavelength of 242 nm. In this study, the iodometric method was used to determine the H_2O_2 concentration. The concentration of H_2O_2 at 352 nm was determined by UV-Visible spectrophotometer after color development for 15 min after 4 mL of 0.1 mol/L potassium iodide (KI) and 100 μL 0.01 mol/L ammonium molybdate ($(\text{NH}_4)_2\text{MoO}_4$) were added into 1 mL reaction sample. The above experiments were carried out in a condensate circulation system, and the temperature of the condensate circulation was set at 23 $^\circ\text{C}$.

2.4. Theoretical calculation

First-principles calculations were performed by vienna *ab initio* simulation package (VASP) [34,35]. The generalized gradient

approximation (GGA) of Perdew-Burke-Ernzerhof (PBE) was used to describe the exchange-correlation functional. The cut-off energy for the plane wave basis was set to 400 eV and a $2 \times 2 \times 1$ Monkhorst-pack mesh was employed. All the structures were fully relaxed (atomic position) up to 10^{-4} eV/Å force minimization and max force of 0.01 eV/Å.

3. Results and discussion

3.1. Photocatalysts synthesis and characterization

The $\text{Bi}_2\text{O}_2\text{CO}_3/\text{CuBi}_2\text{O}_4$ (BOC/CBO) micro rods were *in-situ* synthesis through a one-step hydrothermal method, PVP acted as a carbon source during catalyst synthesis and induced the formation of *in situ* heterojunctions on the catalyst surface. According to the mass of added PVP, which were named CBO-1, CBO-2, and CBO-3, and the construction process of composite photocatalyst was shown in Fig. S1. A schematic depicting the CBO-2 interface was presented in Fig. 1a. In order to analyze the structure of the prepared composites, X-ray diffraction (XRD) was carried out. After synthesis the CBO diffraction peaks in Fig. 1b CuBi_2O_4 monoclinic phase standard card (JCPDS 72-0493) consistent with good, showing it had good crystallinity [36]. Moreover, CBO-2 contained the characteristic peaks of CBO and BOC, and there was no other impurity peak, confirming that CBO and BOC coexisted in the prepared composite catalysts. Noticeably, the intensity of these characteristic peaks of BOC gradually increased with the increasing mass of PVP in the nanocomposites. Subsequently, the morphology and microstructure of the catalysts were investigated. The scanning electron microscopy (SEM) images of the prepared CBO-2 showed nanorods morphology with a length of about 4–6 μm and a diameter of about 100 nm (Fig. S2a). Compared with CBO, the surface of CBO-2 had a large number of loaded particles (red circles) (Fig. S2b). The transmission electron microscopy (TEM) images of CBO-2 showed that many BOC nanosheets were distributed on the surface of CBO (Fig. 1c), while the surface of CBO was relatively smooth (Fig. S3). The high-resolution

transmission electron microscopy (HRTEM) image of CBO-2 clearly showed the (211) plane of CuBi_2O_4 and the (110) plane of $\text{Bi}_2\text{O}_2\text{CO}_3$ with lattice spacings of 0.310 nm and 0.274 nm, respectively. (Fig. 1d). The heterojunction interface with close contact between CBO and BOC could be revealed, which favored the transmission of photogenerated carriers at the interface. The energy dispersive X-ray (EDX) (Fig. S4a) and EDS elemental analysis (Fig. S4b) showed that the CBO-2 has an even distribution of the components C, Bi, Cu, and O. The above results were evidence of the formation of CBO-2 heterojunctions.

The functional groups of the catalyst were investigated using Fourier infrared (FT-IR) (Fig. 1e). Similarly, The CBO-2 also exhibited Fourier infrared spectra (FT-IR) compared to CBO, demonstrating that the formation of heterojunctions did not cause a change in structure. The Raman spectra showed that the characteristic peaks at 116, 180, 253, 383, and 562 cm^{-1} , which could be attributed to the translational vibration of the CuO_4 plane along the Z-axis, the vibration of Cu-Cu, the rotation of two stacked CuO_4 squares in opposite directions, the Bi-O stretching vibration and the in-plane breathing of CuO_4 squares, respectively (Fig. 1f) [37]. Compared with CBO, the Raman characteristic peaks of CBO-2 did not change significantly, which also indicated that the formation of CBO-2 heterojunctions did not alter the crystal structure of CBO. The surface chemical composition and state of the prepared catalyst were further studied by X-ray photoelectron spectroscopy (XPS). As shown in Fig. 2a, for CBO-2, the binding energies of Cu 2p_{3/2} and Cu 2p_{1/2} peaks were 933.6 and 953.3 eV, respectively, and the band gap between Cu 2p_{3/2} and Cu 2p_{1/2} levels was about 20.0 eV, which was consistent with the Cu^{2+} in the standard spectrum of copper oxide [38]. Another two sets of satellite peaks at about 943.0 eV and 963.0 eV, respectively, which might correspond to the open 3d⁹ shell of Cu^{2+} ions [33]. Compared with CBO, the peak of Cu 2p in CBO-2 shifted about 0.3 eV to the higher binding energy, which indicated that the formation of heterojunctions led to the change of electron density between CBO and BOC. As shown in Fig. 2b, compared with CBO, the Bi 4f XPS spectrum of CBO-2 moved 0.2 eV towards higher binding energy,

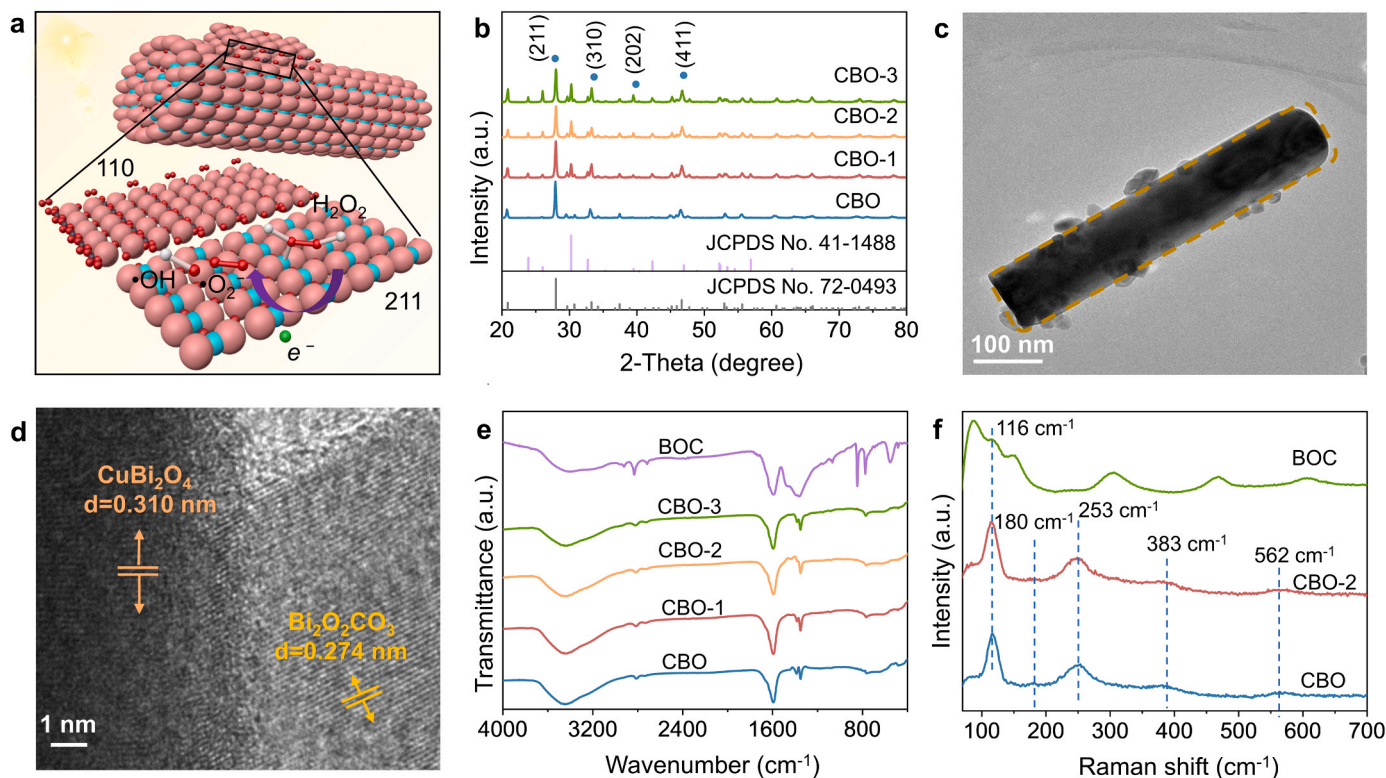


Fig. 1. Characterizations of the prepared catalysts. (a) The BOC/CBO interface structure model; (b) XRD patterns of the prepared samples; (c) TEM and (d) HRTEM images of CBO-2; (e) FT-IR spectra of BOC, CBO, CBO-1, CBO-2, and CBO-3; (f) Raman spectra of BOC, CBO, and CBO-2.

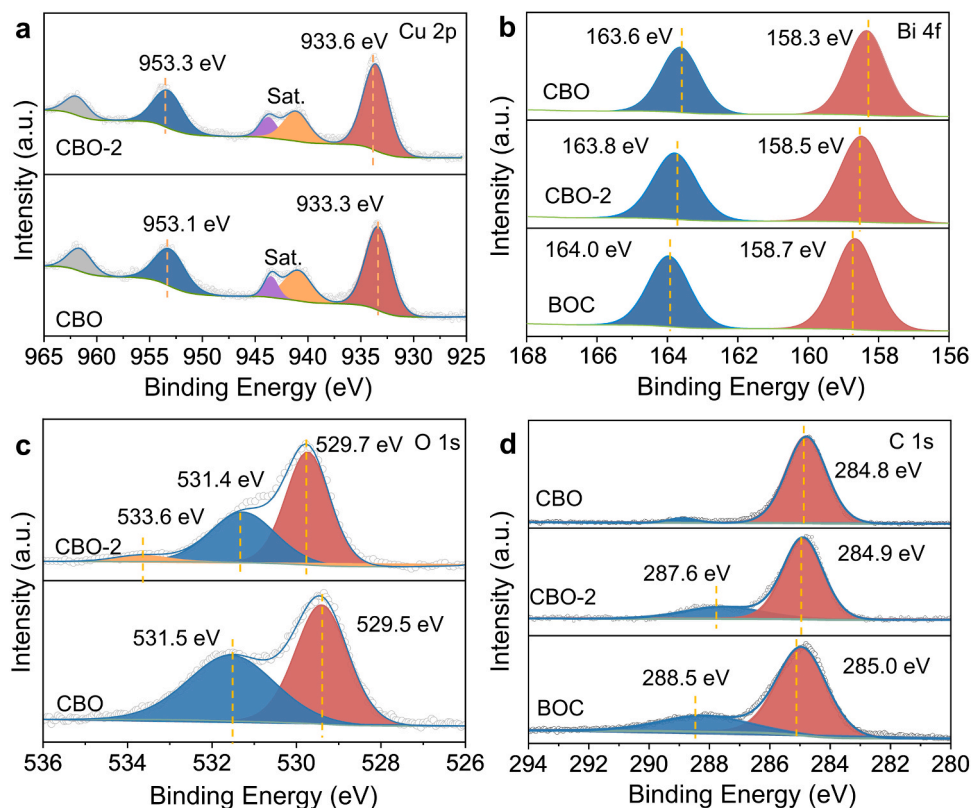


Fig. 2. Chemical state analysis of the catalysts. The high-resolution XPS spectra of the prepared samples: (a) Cu 2p, (b) Bi 4f, (c) O 1s, and (d) C 1s.

which indicated that electrons transfer introduced an internal electric field with direction from CBO to BOC [26]. In the XPS spectrum of O 1s (Fig. 2c), the peaks of CBO-2 at 531.4 eV and 529.7 eV were the

characteristics of surface hydroxyl oxygen and lattice oxygen, respectively [39]. Compared with CBO, the O 1s XPS spectrum of CBO-2 displayed a slightly red shift. The C 1s had peaked at 284.9 eV and

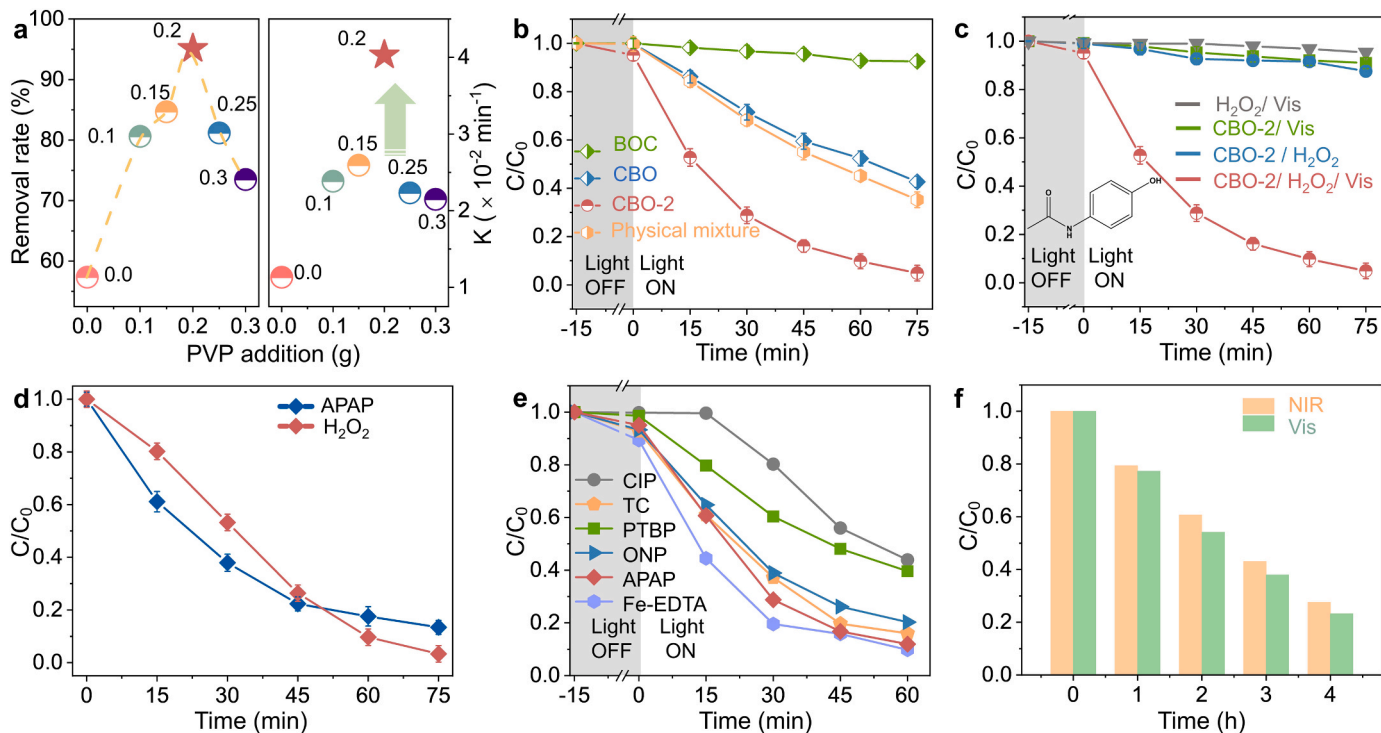


Fig. 3. Catalytic performance assessment. (a) Removal efficiency and First-order rate constants of CBO-x degraded APAP with different content of PVP; (b) Effects of different catalysts on APAP degradation; (c) APAP degradation performance of CBO-2 in different systems; (d) The concentration changes of H₂O₂ during the APAP degradation process; (e) Degradation of diverse pollutants in the CBO-2/H₂O₂/Vis system; (f) TOC degradation of CBO-2 under visible light and NIR light.

287.6 eV, respectively (Fig. 2d), which was from undefined carbon as a reference for energy calibration, and was from the C-O bond in $[\text{CO}_3]^{2-}$ [40]. These results indicated that there was a strong interaction between BOC and CBO, which facilitated the transfer of photogenerated carriers in CBO-2, consequently enhancing the photocatalytic activity.

3.2. Photocatalytic degradation properties

The performance of the photocatalyst was investigated by photodegradation experiments with APAP as the target pollutant under the irradiation of visible light ($\lambda > 420 \text{ nm}$ / $420\text{--}800 \text{ nm}$) and near-infrared light ($\lambda > 800 \text{ nm}$). To optimize the removal rate of APAP, the effects of the amount of PVP added, the amount of catalyst, H_2O_2 , and other key reaction parameters on the degradation rate were studied (Fig. S5). As shown in Fig. 3a, CBO-2 was selected as the model catalyst because of its superior performance (Fig. S6). Under visible light ($420 < \lambda < 800 \text{ nm}$) irradiation (Fig. S7), the rate constant of CBO-2 was 0.0331 min^{-1} . Under visible light ($\lambda > 420 \text{ nm}$) irradiation (Fig. 3b), the rate constant of CBO-2 (0.0403 min^{-1}) was 3.6 times and 36.6 times that of CBO (0.0113 min^{-1}) and BOC (0.0011 min^{-1}) (Fig. S8a–8c). It was worth noting that CBO-2 also showed better APAP removal performance than CBO under near-infrared irradiation (Fig. S8d–8f), and the rate constant of CBO-2 (0.0255 min^{-1}) was 2.3 times and 21.2 times that of CBO (0.0111 min^{-1}) and BOC (0.0012 min^{-1}). In addition, the physical mixture (prepared by ultrasonically mixing CBO and BOC) was significantly poor APAP degradation properties compared with CBO-2, indicating that the closer interfacial interaction of *in-situ* synthesized composite catalyst might promote interfacial electron transfer. The photo-Fenton-like activity of CBO-2 was also assessed by the degradation of APAP (Fig. 3c). When only CBO-2 or Vis/NIR/ H_2O_2 was present, almost no obvious degradation was observed (Fig. S9), indicating that the adsorption and degradation ability of CBO-2 could be negligible and that the combination of H_2O_2 and light had no oxidation capacity in the

absence of the catalyst. Nearly no degradation of APAP occurred in the presence of CBO-2/ H_2O_2 or CBO-2/Vis. In contrast, CBO-2/Vis/ H_2O_2 removed 95% of APAP within 75 min, suggesting that the photo-Fenton-like method could effectively activate H_2O_2 to oxidize APAP. Moreover, H_2O_2 concentration in the process of APAP degradation was studied. As shown in Fig. 3d, H_2O_2 concentration decreased simultaneously with APAP concentration, indicating that the process of APAP degradation was by activation of H_2O_2 . As shown in Fig. S10 and Table S1, the k -value of the different catalytic systems for APAP degradation was calculated. Notably, the CBO-2 exhibited the best catalytic performance among all the recently reported catalysts. Furthermore, the CBO-2/Vis/ H_2O_2 system could also be applied to the removal of other organic contaminants (such as CIP, TC, ONP, etc.) as well as complex heavy metal contaminants (such as Fe-EDTA, Cu-EDTA, etc.) (Fig. 3e), demonstrating its remarkable activity and wide adaptability. Subsequently, the total organic carbon (TOC) removal rate represented the degree of mineralization of pollutants. TOC removal ability of CBO-2 under visible and near-infrared light irradiation was 76.6% and 73.5%, respectively (Fig. 3f), illustrating that APAP was finally mineralized into CO_2 , H_2O , and a few intermediates. Besides, cyclic stability was also a key factor for the practical application of photocatalysts. XRD, FT-IR, and XPS analysis result showed that there was almost no difference between the samples after the reaction and the samples before the reaction, and the same crystal structure properties and chemical state. CBO-2 could retain its photocatalytic properties and morphology well after four consecutive photocatalytic cycles, indicating that the photocatalyst had good reusability and stability (Fig. S11).

The contribution of the active species was evaluated by the extent to which the degradation was inhibited by the addition of the sacrifice agent. To acquire the major active species for the degradation of APAP, mannitol, benzoquinone (PBQ), and carotene were used to catch $\bullet\text{OH}$, $\bullet\text{O}_2^-$, and $^1\text{O}_2$. (Fig. 4a). When mannitol was added to the solution, the photodegradation was largely inhibited, explaining that $\bullet\text{OH}$ was the

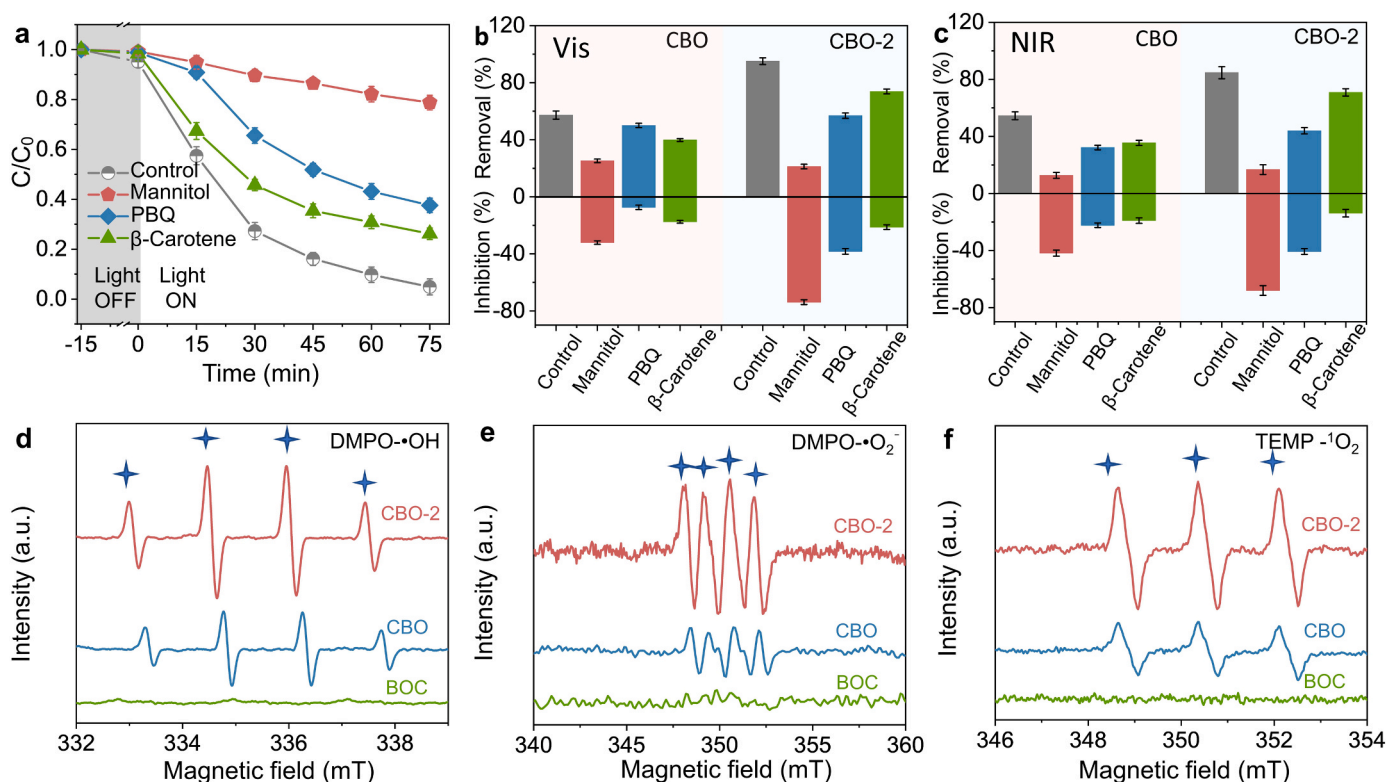


Fig. 4. Identification of reactive species in photodegradation process. (a) Experiments on the capture of active species with different scavenger; Removal rate and inhibition rate of APAP degradation on CBO-2 photocatalyst with different scavenger (b) in visible light and (c) NIR light; ESR spectra of BOC, CBO, and CBO-2 in the existence of (d) DMPO- $\bullet\text{OH}$, (e) DMPO- $\bullet\text{O}_2^-$, and (f) TEMP- $^1\text{O}_2$, respectively.

major active substance in the APAP degradation (Fig. 4b-c). At the same time, PBQ and carotene had a weak inhibitory effect on CBO-2/Vis/ H_2O_2 system, indicating that $\bullet\text{O}_2^-$ and $^1\text{O}_2$ had a slight impact on the APAP degradation. Electron spin resonance (ESR) technology detected the active components in the process of pollutant degradation (Section S2 and Fig. 4d-f). In this study, 2,2,6,6-tetramethylpiperidine (TEMP) and 5,5-dimethyl-1-pyrroline N-oxide (DMPO) were used as collectors to capture signals of $^1\text{O}_2$, $\bullet\text{O}_2^-$, and $\bullet\text{OH}$. The $\bullet\text{OH}$ signal of CBO-2/Vis/ H_2O_2 was significantly stronger than that of CBO, BOC, which further confirmed the effectiveness of heterojunction formation in improving the H_2O_2 activation activity. In addition, in the presence of H_2O_2 , $\bullet\text{OH}$, $\bullet\text{O}_2^-$, and $^1\text{O}_2$ signals were significantly stronger than the light catalytic system (Fig. S12). It was shown that hydroxyl radicals from the H_2O_2 decomposition process, rather than the photocatalytic process. The above results indicated that heterojunction creation could activate H_2O_2 more effectively, and produce more $\bullet\text{OH}$ (Fig. S12).

3.3. Mechanism of photocatalytic degradation enhanced by interfacial interaction

To gain insight into the mechanism of photocatalytic H_2O_2 activation, light absorption, charge separation, and transfer of CBO-2 were investigated. Firstly, the optical absorption capacity of CBO-2 was studied by UV-Visible diffuse reflection spectroscopy. As shown in Fig. 5a, CBO exhibited strong absorption in both UV and visible wavelength ranges ending at 820 nm. While BOC had an absorption edge of only about 420 nm, which could be attributed to its narrow band gap. The formation of CBO-2 heterojunction enhanced the absorption capacity of CBO-2 in the near-infrared region, showing obvious redshift enhancement. Meanwhile, according to the relationship diagram between $(\alpha h\nu)^{1/2}$ or $(\alpha h\nu)^2$ and photon energy ($h\nu$), it was possible to determine the direct transition semiconductor's band gap energy (E_g) (Fig. S13). As shown in the inset of Fig. 5a, the energy bands (E_g) of BOC and CBO were 3.1 eV and 1.78 eV, respectively. Valence band X-ray photoelectron spectroscopy (XPS) of CBO and BOC showed that VB positions were 1.18 eV and 2.66 eV, respectively (Fig. 5b). According to

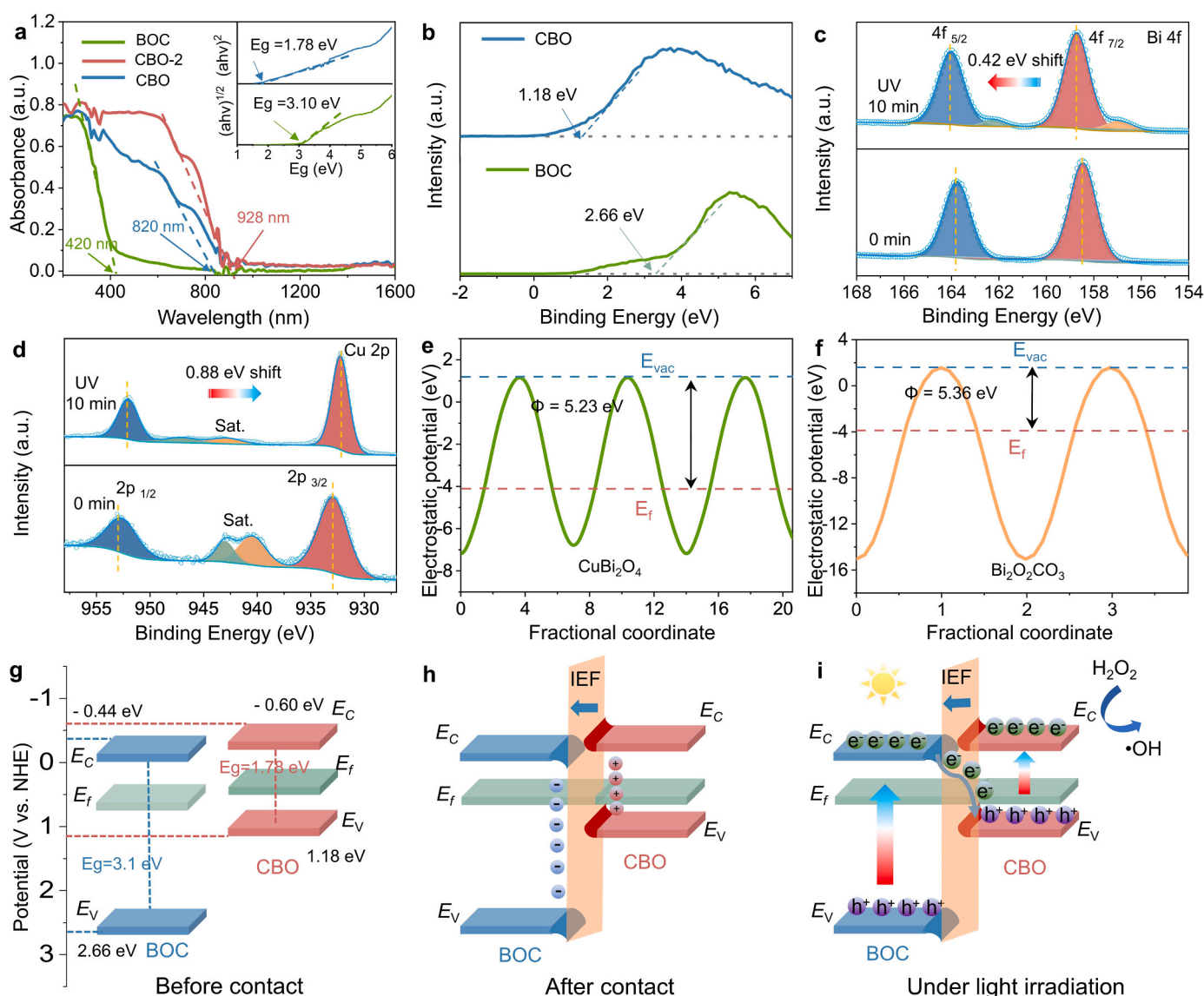


Fig. 5. Electron transfer between CBO and BOC and the photocatalytic mechanism of S-scheme heterojunction. (a) UV/Vis-NIR diffuse reflectance spectra (inset: bandgap energy); (b) Valence band spectra of CBO and BOC; High-resolution (c) Bi 4f and (d) Cu 2p XPS spectra of CBO-2 samples tested in darkness and under illumination; The electrostatic potentials of (e) CBO (211) and (f) BOC (110) facets; (g-i) Schematic illustration of BOC/CBO heterojunction: internal electric field (IEF)-induced charge transfer, separation, and the formation of S-scheme heterojunction under UV/Vis-NIR light irradiation for activation of H_2O_2 .

the equation $E_{CB} = E_{VB} - E_g$, CBO and BOC were calculated to be -0.60 eV and -0.44 eV, respectively (vs. NHE) [32].

In-situ irradiation XPS spectroscopy was one of the effective means to study electron flow direction and chemical state in heterojunction. The heterojunction was photoexcited and electrons were transferred between the two semiconductors, resulting in a change in the electron cloud density of the semiconductor, which showed a shift in the characteristic peaks in XPS [30,41]. After CBO-2 was irradiated by visible light, the characteristic peak of Bi 4f shifted to the high energy region (Fig. 5c), indicating that the density of the electron cloud around the Bi atom decreased, that was, the electron shell of the Bi atom had lost electrons. Meanwhile, in the Cu 2p high-resolution XPS spectrum (Fig. 5d), the characteristic peak shifted to the low energy region, which proved that the density of the electron cloud around the Cu atom increased, indicating that the electron shell of the Cu atom had accumulated. All ISI-XPS results manifested that with the irradiation of light, the electron flowed from BOC to CBO through the CBO-2 interface.

In order to further study the charge transfer path within

semiconductor heterostructures and interface interaction of CBO-2, electronic properties were calculated based on DFT (Fig. 5e-f). The work functions of BOC (110) and CBO (211) were calculated to be 5.36 eV and 5.23 eV *versus* vacuum level, respectively, indicating that the calculated CBO had a higher Fermi level than BOC [42]. When CBO and BOC were in contact (Fig. 5g-h), the electrons tend to flow from CBO to BOC to reach the same Fermi energy level. The BOC component close to the interface was negatively charged, while the CBO part near the interface was positively charged due to electron migration [41]. Internal electric field (IEF) was generated on the CBO-2 interface from CBO to BOC, making the energy bands of BOC and CBO bend. Under light excitation (Fig. 5i), electrons in VB of BOC and CBO jumped to their CB. Driven by the interface IEF and bending band, the photogenerated electrons in the CB of the BOC spontaneously slid towards the CBO and combined with the holes in the VB of the CBO. The electron-rich CBO acted as the active site to provide electrons to the activated H_2O_2 molecule to generate $\bullet OH$. Finally, these active species effectively degraded APAP through the advanced oxidation process.

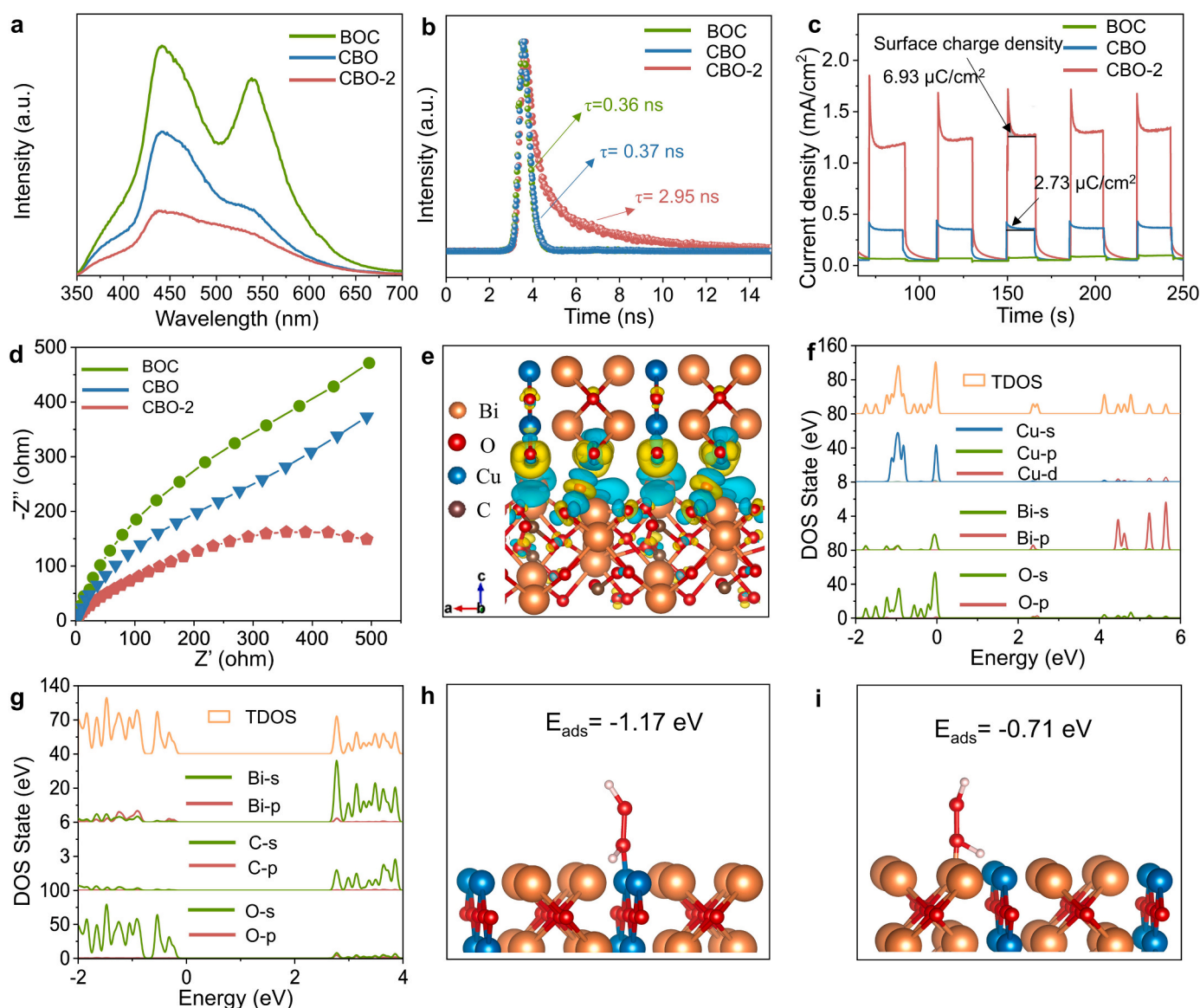


Fig. 6. Investigation of photoexcited charges transportation. (a) Steady-state PL spectra excited at 325 nm, (b) Time-resolved PL decay spectra, (c) Photocurrent responses, and (d) EIS Nyquist plots of BOC, CBO, and CBO-2; (e) Difference charge density image for the interface of CBO-2, ultramarine and yellow areas represented electron accumulation and consumption, respectively; State density of CBO (f) and BOC (g); Optimized structures of H_2O_2 molecule adsorbed on (h) Cu atom, (i) Bi atom of CBO. The blue, red, yellow, and pink spheres stand for Cu, O, Bi, and H atoms, respectively.

To further prove the effective charge separation of CBO-2 heterojunction, we conducted a steady-state photoluminescence (PL) emission test. In general, PL analysis was mainly used to reveal the migration, transfer, and separation efficiency of photo-excited electrons and holes in semiconductors [43]. The lower the PL intensity, the lower the recombination rate of the electron-hole pair of the photocatalyst [44]. As shown in Fig. 6a, the emission spectra of BOC, CBO, and CBO-2 under 325 nm excitation. Compared with CBO, the PL emission intensity of CBO-2 decreased rapidly, and the formation of heterojunction inhibited the recombination of photogenerated electron-hole pairs. At the same time, the strength of the defect peak of BOC was weakened, which reduced the electron-hole recombination at the defect. Besides, in order to evaluate the carrier lifetime of the prepared photocatalyst, time-resolved photoluminescence (TRPL) was employed. The carrier lifetime of CBO-2 was the longest ($\tau_{ave}=2.95$ ns) (Table S2), indicating that more photogenerated electrons could participate in the activation of H_2O_2 (Fig. 6b). It was noteworthy that CBO-2 showed the highest photocurrent, indicating that the photogenerated electrons and holes at the interface between BOC and CBO were effectively separated (Fig. 6c). It was well known that the surface charge density was proportional to the number of positive charges accumulated on the surface [45]. By integrating the measured transient photocurrent density minus the steady-state values of photocurrent with respect to time, the surface charge density of CBO-2 was more than twice that of CBO, indicating that more charges were involved in the activation of H_2O_2 on the surface of CBO-2. After adding H_2O_2 , the photocurrent density decreased significantly (Fig. S14a), because the electrons transferred to the material surface participated in the Fenton-like reaction. Subsequently, the electrochemical impedance spectroscopy (EIS) showed that the arc radius observed in CBO-2 was small (Fig. 6d), indicating that the heterojunction structure was conducive to reducing the charge transfer resistance. In addition, the radius of the EIS curve obtained by CBO-2 with the addition of H_2O_2 became larger (Fig. S14b), which was because Fenton-like reactions consumed the electrons generated, and they promoted carrier separation [46]. The above results further proved that the heterojunction structure could separate and transfer charge rapidly to improve the activation efficiency of H_2O_2 .

The atomic structure model of CBO-2 heterojunction with Cu-O-Bi transition layer at the interface was established based on DFT calculation (Fig. S15). In order to intuitively showed the electron transfer direction of the CBO-2 heterojunction interface, it was calculated the charge density difference. As shown in Fig. 6e, the BOC in the CBO-2 heterojunction interface was acquiring electrons, which intuitively proved the electron transfer from CBO to BOC. In order to further understand the working mechanism of the Cu-O-Bi transition layer, we also calculated the partial density of states (PDOS) of CBO and BOC (Fig. 6f-g). For CBO, the highest occupied orbital level for CBO was formed by the O 2p and Cu 4d hybrid orbital, and the lowest unoccupied molecular orbital level was the Bi 6s orbitals. These results implied that the photoinduced electrons transferred from the VBM formed by the O 2p and Cu 4d hybrid orbital to the CBM of Bi 6s hybrid orbitals. As for BOC, the VBM and CBM were composed of O2p and Bi 6s orbitals, the electrons transferred from the VB edge of O 2p to the CB edge of Bi 6s. For CBO-2, electrons would transfer from CBO to the edge of the low valence band of BOC through the interface state. Considering that the interface state come from the Cu-O-Bi transition layer, we could conclude that the electrons transferred from CBO to BOC [47]. These results were completely consistent with the above difference charge density results. Obviously, the photo-induced carrier transport follows the S-type sliding path, which meant that there was an S-type heterojunction between BOC and CBO. This unique S-type charge transfer effectively separated the photogenerated electron-hole pairs and enhances the activation efficiency of H_2O_2 . Furthermore, the adsorption of H_2O_2 by photocatalyst was an important step to activate H_2O_2 [41]. BET surface area of CBO and CBO-2 was 90.2 and 126.2 m^2/g , respectively (Fig. S16, Table S3), CBO-2 with a high specific surface area could provide more active sites.

As shown in Fig. 6h-i, we compared the optimization models of H_2O_2 molecules adsorbed on the Cu site and Bi site of CBO. Obviously, the adsorption energy of H_2O_2 at the Cu site (-1.17 eV) was more negative than that at Bi site (-0.71 eV), indicating that the adsorption of H_2O_2 on Cu site was more stable than that on Bi site. The results also showed that the Cu site was conducive to the adsorption and activation of the H_2O_2 molecule. The above research indicated that the unique heterostructure was more conducive to the adsorption and activation of H_2O_2 .

3.4. Degradation pathway and toxicity estimation of APAP intermediates with practical application

The application of photocatalysis technology in actual wastewater treatment had been affected by many factors, such as dissolved natural organic matter and anions in wastewater. An experimental comparison was depicted in Fig. S17. It was worth noting that the rate of APAP degradation was unaffected by the addition of common background chemicals including HA, Cl^- , and SO_4^{2-} to water (Fig. S17a), deionized water, tap water, and natural water (Nankai University Matti Lake, Fig. S17b). As the pollutant concentration increased or decreased, the degradation rate could still be more than 75% (Fig. S17c-17d). The system based on CBO-2/Vis/ H_2O_2 maintained high reactivity in the range of pH 3–9 (Fig. S18a-18b). The change of system pH under different initial pH values was further investigated (Fig. S18c). As the reaction time increased, the system became acidic. Possible causes included the production of small organic acids and the release of protons during APAP degradation [48]. In order to deeply analyze the degradation process of APAP, the intermediates of APAP were analyzed by LC-MS (Table S4). Based on the above results, we proposed two possible ways to degrade APAP (Fig. S19) and the mass spectra of the intermediates (Fig. S20). The degradation pathway of acetaminophen showed that $\bullet OH$ had a tendency to attack the OH functional group of the APAP, which meant that the hydroxylation reaction of APAP should be the main mechanism of APAP degradation [48]. This attack produced hydroquinone. On the one hand, the hydroxy group of hydroquinone was methylated and oxidized to produce 1,4-benzoquinone (P4) [49]. On the other hand, hydroquinone was converted to benzoic acid (P5) [50]. This substance further broke off the aromatic ring and decomposed into acids or alcohols. These substances were then completely mineralized and converted into carbon dioxide.

Subsequently, the toxicity evaluation software tool (T.E.S.T.) was used to evaluate the acute toxicity, bioaccumulation factors, and mutagenicity of the above degradation products compared with APAP using the quantitative structure-activity relationship (QSAR) method. It was well known that LD_{50} was the minimum number of bacteria or toxins required for half of the death of an animal. As shown in Fig. 7a, the LD_{50} of APAP to rats was 1684 mg/kg, which was far lower than almost all final degradation products (except P9). It was evident from Fig. 7b that the bioaccumulation factors of the four products P6, P7, P8, and P9 were significantly lower than those of APAP, and their bioaccumulation factors had decreased by 91.3%, 18.5%, 65.3%, and 88.4%, respectively. It could be seen from Fig. 7c that APAP was mutagenic positive, and the reaction system reduced the mutagenicity of the final product to "negative mutagenicity". These facts showed that this degradation process could effectively reduce and weaken the acute toxicity, bioaccumulation factors, and mutagenicity of APAP. In order to investigate the adaptability of the CBO-2/Vis/ H_2O_2 system in practical application, we set up a continuous flow experiment (Section S3 and Fig. 7d-e). The CBO-2 membrane was prepared by vacuum filtration using a polyvinylidene fluoride (PVDF) membrane as the support film. The Catalyst was firmly attached to the membrane surface to prevent it from falling off during the catalytic reaction (Fig. 7f-h). The rhodamine B solution flowed into the reactor from the upper end. The flow rate was 4 mL/min, and it was collected at the other end. As shown in Fig. 7i, the system showed stable and efficient degradation of rhodamine B in the next 4 h. In the continuous 4 h experiment, the collected solution was

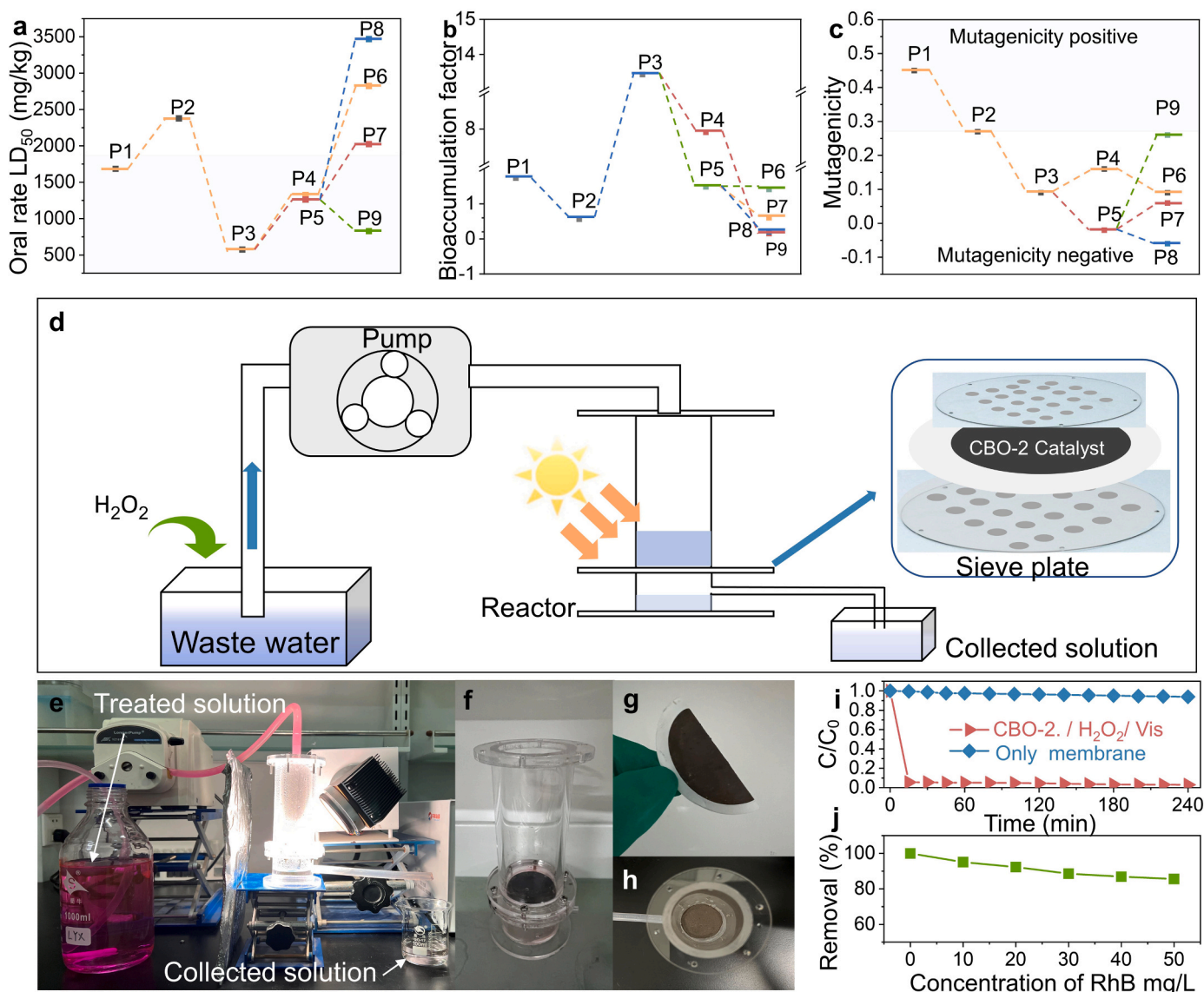


Fig. 7. Toxicity assessment of pollutants and practical application. (a) Acute toxicity, (b) Bioaccumulation factors, and (c) Mutagenicity of APAP and degradation products; (d) Schematic illustration of the experiment set; (e) Diagram of continuous flow test facility; (f) Reactor installation diagram; (g-h) The catalyst-loaded membrane; (i) The removal of rhodamine B by the continuous flow set; (j) Degradation rates of rhodamine B at different concentrations.

colorless, which proved rhodamine B was effectively degraded. And, at various concentrations, an effective elimination effect could be obtained. (Fig. 7j). In addition, in the case of the osmotic membrane alone (without catalyst), it was found that the solution flowing from the lower end was no different from the solution flowing from the upper end, ruling out the adsorption of rhodamine B by the osmotic membrane. (Fig. S21). This experiment not only showed that the CBO-2/Vis/H₂O₂ system had good and stable catalytic performance but also had certain practical application prospects.

4. Conclusion

In summary, an S-scheme Bi₂O₂CO₃/CuBi₂O₄ heterojunction was successfully *in-situ* synthesized. The construction of heterojunction could enhance the photocatalytic activation of H₂O₂, showing the excellent photocatalytic capacity for the degradation of organic pollutants and complex heavy metal pollutants. The photocatalytic degradation rate constants of CBO-2 for APAP were 3.6 times and 36.6 times that of CBO and BOC, respectively. Under near-infrared irradiation, the photocatalytic degradation rate constants of CBO-2 for APAP were 2.3

times and 21.2 times that of CBO and BOC, respectively. The computational analysis confirmed that the adsorption of H₂O₂ at the Cu site in the CBO-2 heterojunction was more stable than the Bi site. The ISI-XPS and DFT calculations showed that there was an interface interaction between CBO and BOC. Besides, driven by the interface IEF and bending band, the photogenerated electrons in the CB of BOC slid spontaneously along the S-shaped path towards the VB of the CBO. Electrochemical and photochemical results further revealed that the charge separation and transfer process was effectively enhanced, hence increasing the number of electrons transferred from the photocatalyst to H₂O₂ and resulting in the production of •OH. Moreover, two possible photodegradation pathways of APAP were proposed through LC-MS analysis, and it was found that the para-hydroxyl functional groups in APAP were vulnerable to ROS attacks. Toxicity in water showed that CBO-2 did not produce highly toxic products during the photodegradation of APAP. This work might not only be applicable to the actual water remediation but also provide a new way to enhance the photocatalytic activation of H₂O₂ by S-type heterojunction under near-infrared light.

CRediT authorship contribution statement

Jinyong Qu: Investigation, Data curation, Writing – original draft, Writing – review & editing. **Yueshuang Mao, Tao Zhang and Pengfei Wang:** Investigation, Data curation. **Dongpeng Zhang:** Designed the research, Writing – review & editing. **Yanxiao Li:** Writing – review & editing. **Yi Li:** Writing – review & editing. **Sihui Zhan:** Conceptualization, Supervision, Funding acquisition, Resources, Writing – review & editing.

Declaration of Competing Interest

The authors declare no competing interests.

Data Availability

Data will be made available on request.

Acknowledgements

The authors gratefully acknowledge the financially support by the Natural Science Foundation of China as general projects (grant Nos. 22225604, 22076082, and 22176140), the Frontiers Science Center for New Organic Matter (grant No. 63181206), and Haihe Laboratory of Sustainable Chemical Transformations.

Appendix A. Supporting information

Supplementary data associated with this article can be found in the online version at doi:10.1016/j.apcatb.2023.123246.

References

- [1] R.X. Guo, X.H. Cai, H.W. Liu, Z. Yang, Y.J. Meng, F.J. Chen, Y.J. Li, B.D. Wang, In situ growth of metal-organic frameworks in three-dimensional aligned lumen arrays of wood for rapid and highly efficient organic pollutant removal, *Environ. Sci. Technol.* 53 (2019) 2705–2712.
- [2] A.K. Ghattas, F. Fischer, A. Wick, T.A. Ternes, Anaerobic biodegradation of (emerging) organic contaminants in the aquatic environment, *Water Res.* 116 (2017) 268–295.
- [3] S.Y. Wu, W. Wu, J.N. Fan, L.P. Zhang, Y. Zhong, H. Xu, Z.P. Mao, Rapid activation of peroxymonosulfate with iron(III) complex for organic pollutants degradation via a non-radical pathway, *Water Res.* 233 (2023), 119725.
- [4] J.K. Lin, W.J. Tian, Z.Y. Guan, H.Y. Zhang, X.G. Duan, H. Wang, H.Q. Sun, Y. F. Fang, Y.P. Huang, S.B. Wang, Functional carbon nitride materials in photo-Fenton-like catalysis for environmental remediation, *Adv. Funct. Mater.* 32 (2022), 2201743.
- [5] D.Z. Kong, Y.M. Zhao, X.R. Fan, X.S. Wang, J.X. Li, X.X. Wang, J. Nan, J. Ma, Reduced graphene oxide triggers peracetic acid activation for robust removal of micropollutants: the role of electron transfer, *Environ. Sci. Technol.* 56 (2022) 11707–11717.
- [6] X.Q. Shen, F. Xiao, H.Y. Zhao, Y. Chen, C. Fang, R. Xiao, W.H. Chu, G.H. Zhao, In situ-formed PdFe nanoalloy and carbon defects in cathode for synergic reduction-oxidation of chlorinated pollutants in electro-Fenton process, *Environ. Sci. Technol.* 54 (2020) 4564–4572.
- [7] M.E. Kateb, C. Trellu, A. Darwich, M. Rivallin, M. Bechelany, S. Nagarajan, S. Lacour, N. Bellakhal, G. Lesage, M. Heran, M. Cretin, Electrochemical advanced oxidation processes using novel electrode materials for mineralization and biodegradability enhancement of nanofiltration concentrate of landfill leachates, *Water Res.* 162 (2019) 446–455.
- [8] V.I. Parvulescu, F. Epron, H. Garcia, P. Granger, Recent progress and prospects in catalytic water treatment, *Chem. Rev.* 122 (2022) 2981–3121.
- [9] Y.X. Ye, J.H. Pan, F.Y. Xie, L. Gong, S.M. Huang, Z.F. Ke, F. Zhu, J.Q. Xu, G. F. Ouyang, Highly efficient photosynthesis of hydrogen peroxide in ambient conditions, *Proc. Natl. Acad. Sci. U. S. A.* 118 (2021), e2103964118.
- [10] Y. Ahmed, J.X. Zhong, L.Z. Wang, L.Z. Wang, Z.G. Yuan, J.H. Guo, Simultaneous removal of antibiotic resistant bacteria, antibiotic resistance genes, and micropollutants by FeS₂@GO-based heterogeneous Photo-Fenton process, *Environ. Sci. Technol.* 56 (2022) 15156–15166.
- [11] W. Miao, Y. Liu, X.Y. Chen, Y.X. Zhao, S. Mao, Tuning layered Fe-doped g-C₃N₄ structure through pyrolysis for enhanced Fenton and photo-Fenton activities, *Carbon* 159 (2020) 461–470.
- [12] Y.F. Chen, H.C. Vu, C.J. Miller, S. Garg, D. Pan, T.D. Waite, Comparative experimental and computational studies of hydroxyl and sulfate radical-mediated degradation of simple and complex organic substrates, *Environ. Sci. Technol.* 56 (2022) 8819–8832.
- [13] H.Y. Zhou, H. Zhang, Y.L. He, B.K. Huang, C.Y. Zhou, G. Yao, B. Lai, Critical review of reductant-enhanced peroxide activation processes: Trade-off between accelerated Fe³⁺/Fe²⁺ cycle and quenching reactions, *Appl. Catal. B Environ.* 286 (2021), 119900.
- [14] Y.S. Mao, P.F. Wang, D.P. Zhang, Y.G. Xia, Y. Li, W.L. Zeng, S.H. Zhan, J. C. Crittenden, Accelerating Fe^{III}-aqua complex reduction in an efficient solid-liquid-interfacial Fenton reaction over the Mn-CN_H Co-catalyst at near-neutral pH, *Environ. Sci. Technol.* 55 (2021) 13326–13334.
- [15] C.C. Ling, X.F. Liu, H. Li, X.B. Wang, H.Y. Gu, K. Wei, M.Q. Li, Y.B. Shi, H.J. Ben, G. M. Zhan, C. Liang, W.J. Shen, Y.L. Li, J.C. Zhao, L.Z. Zhang, Atomic-layered Cu₅ nanoclusters on FeS₂ with dual catalytic sites for efficient and selective H₂O₂ activation, *Angew. Chem. Int. Ed.* 61 (2022), e202200670.
- [16] T.Y. Li, L.F. Ge, X.X. Peng, W. Wang, W.X. Zhang, Enhanced degradation of sulfamethoxazole by a novel Fenton-like system with significantly reduced consumption of H₂O₂ activated by g-C₃N₄/MgO composite, *Water Res.* 190 (2021), 116777.
- [17] Y. Yin, R.L. Lv, X.Y. Li, L. Lv, W.M. Zhang, Exploring the mechanism of ZrO₂ structure features on H₂O₂ activation in Zr-Fe bimetallic catalyst, *Appl. Catal. B Environ.* 299 (2021), 120685.
- [18] W.Q. Li, Y.X. Wang, J.Q. Chen, N.N. Hou, Y.M. Li, X.C. Liu, R.R. Ding, G.N. Zhou, Q. Li, X.G. Zhou, Y. Mu, Boosting photo-Fenton process enabled by ligand-to-cluster charge transfer excitations in iron-based metal organic framework, *Appl. Catal. B Environ.* 302 (2022), 120882.
- [19] X.M. Xu, Y.M. Zhang, Y. Chen, C.H. Liu, W.J. Wang, J.J. Wang, H.T. Huang, J. Y. Feng, Z.S. Li, Z.G. Zou, Revealing *OOH key intermediates and regulating H₂O₂ photoactivation by surface relaxation of Fenton-like catalysts, *Proc. Natl. Acad. Sci. U. S. A.* 119 (2022), e2205562119.
- [20] L.N. Su, P.F. Wang, X.L. Ma, J.H. Wang, S.H. Zhan, Regulating local electron density of iron single sites by introducing nitrogen vacancies for efficient photo-Fenton, *Process, Angew. Chem. Int. Ed.* 60 (2021) 21261–21266.
- [21] D.P. Zhang, P.F. Wang, J.H. Wang, Y. Li, Y.G. Xia, S.H. Zhan, Tailoring of electronic and surface structures boosts exciton-triggering photocatalysis for singlet oxygen generation, *Proc. Natl. Acad. Sci. U. S. A.* 118 (2021), e2114729118.
- [22] J. Li, W.F. Pan, Q.Y. Liu, Z.Q. Chen, Z.J. Chen, X.Z. Feng, H. Chen, Interfacial engineering of Bi₁₉Br₃S₂₇ nanowires promotes metallic photocatalytic CO₂ reduction activity under near-infrared light irradiation, *J. Am. Chem. Soc.* 143 (2021) 6551–6559.
- [23] Q.W. Wang, D.Y. Xu, Y.L. Dong, S.X. Pang, L.J. Zhang, G.M. Zhang, L.Y. Lv, X. Y. Liu, Y.G. Xia, L.C. Campos, Z.J. Ren, P.F. Wang, Unsaturated Nd-Bi dual-metal sites enable efficient NIR light-driven O₂ activation for water purification, *Appl. Catal. B Environ.* 319 (2022), 121924.
- [24] F. Zaera, Designing sites in heterogeneous catalysis: are we reaching selectivities competitive with those of homogeneous catalysts? *Chem. Rev.* 122 (2022) 8594–8757.
- [25] D.P. Zhang, Y.X. Li, Y. Li, S.H. Zhan, Towards single-atom photocatalysts for future carbon-neutral application, *SmartMat* 3 (2022) 417–446.
- [26] Z. Xing, J. Hu, M. Ma, H. Lin, Y.M. An, Z.H. Liu, Y. Zhang, J.Y. Li, S.H. Yang, From one to two: In situ construction of an ultrathin ²D–²D closely bonded heterojunction from a single-phase monolayer nanosheet, *J. Am. Chem. Soc.* 141 (2019) 19715–19727.
- [27] W. Li, C. Liu, C.K. Gu, J.H. Choi, S. Wang, J. Jiang, Interlayer charge transfer regulates single-atom catalytic activity on electrode/graphene 2D heterojunctions, *J. Am. Chem. Soc.* 145 (2023) 4774–4783.
- [28] S.K. Xue, W.Q. Huang, W. Lin, W.D. Xing, M. Shen, X.Y. Ye, X.C. Liang, C. Yang, Y. D. Hou, Z.Y. Yu, X.C. Wang, Interfacial engineering of lattice coherency at ZnO-ZnS photocatalytic heterojunctions, *Chem. Catal.* 2 (2022) 125–139.
- [29] X.X. Chen, W.Y. Fu, Z.C. Yang, Y.L. Yang, Y.J. Li, H. Huang, X.H. Zhang, B.C. Pan, Enhanced H₂O₂ utilization efficiency in Fenton-like system for degradation of emerging contaminants: oxygen vacancy-mediated activation of O₂, *Water Res.* 230 (2023), 119562.
- [30] J.X. Low, B.Z. Dai, T. Tong, C.J. Jiang, J.G. Yu, In situ irradiated X-ray photoelectron spectroscopy investigation on a direct Z-scheme TiO₂/CdS composite film photocatalyst, *Adv. Mater.* 31 (2019), e1802981.
- [31] Z.Y. Wang, Y. Huang, L. Chen, M.J. Chen, J.J. Cao, W.K. Ho, S.C. Lee, In situ g-C₃N₄ self-sacrificial synthesis of a g-C₃N₄/LaCoO₃OH heterostructure with strong interfacial charge transfer and separation for photocatalytic NO removal, *J. Mater. Chem. A* 6 (2018) 972–981.
- [32] P.F. Xia, S.W. Cao, B.C. Zhu, M.J. Liu, M.S. Shi, J.G. Yu, Y.F. Zhang, Designing a 0D/2D S-scheme heterojunction over polymeric carbon nitride for visible-light photocatalytic inactivation of bacteria, *Angew. Chem. Int. Ed.* 59 (2020) 5218–5225.
- [33] W.L. Shi, F. Guo, S.L. Yuan, In situ synthesis of Z-scheme Ag₃PO₄/CuBi₂O₄ photocatalysts and enhanced photocatalytic performance for the degradation of tetracycline under visible light irradiation, *Appl. Catal. B Environ.* 209 (2017) 720–728.
- [34] G. Kresse, D. Joubert, Ultrasoft pseudopotentials to the projector augmented-wave method, *Phys. Rev. B Condens. Matter* 59 (1999).
- [35] G. Kresse, J. Furthmüller, Efficiency of ab-initio total energy calculations for metals and semiconductors using a plane-wave basis set, *Comput. Mater. Sci.* (1996) 15–50.
- [36] Y.P. Wang, C. Liu, Y.T. Zhang, W.D. Meng, B. Yu, S.Y. Pu, D.H. Yuan, F. Qi, B.B. Xu, W. Chu, Sulfate radical-based photo-Fenton reaction derived by CuBi₂O₄ and its composites with alpha-Bi₂O₃ under visible light irradiation: Catalyst fabrication, performance and reaction mechanism, *Appl. Catal. B Environ.* 235 (2018) 264–273.

- [37] S. Yuvaraj, K. Karthikeyan, D. Kalpana, Y.S. Lee, R.K. Selvan, Surfactant-free hydrothermal synthesis of hierarchically structured spherical CuBi_2O_4 as negative electrodes for Li-ion hybrid capacitors, *J. Colloid Interface Sci.* 469 (2016) 47–56.
- [38] P.S. Li, J.H. Bi, J.Y. Liu, Q.G. Zhu, C.J. Chen, X.F. Sun, J.L. Zhang, B.X. Han, In situ dual doping for constructing efficient CO_2 -to-methanol electrocatalysts, *Nat. Commun.* 13 (2022) 1965.
- [39] Q. Chen, H.M. Long, M.J. Chen, Y.F. Rao, X.W. Li, Y. Huang, In situ construction of biocompatible Z-scheme $\alpha\text{-Bi}_2\text{O}_3/\text{CuBi}_2\text{O}_4$ heterojunction for NO removal under visible light, *Appl. Catal. B Environ.* 272 (2020), 119008.
- [40] Y.X. Zhang, X. Chen, Y.H. Ye, J.Z. Chen, Photocatalytic oxygen reduction reaction over copper-indium-sulfide modified polymeric carbon nitride S-scheme heterojunction photocatalyst, *J. Catal.* 419 (2023) 9–18.
- [41] F.Y. Xu, K. Meng, B. Cheng, S.Y. Wang, J.S. Xu, J.G. Yu, Unique S-scheme heterojunctions in self-assembled $\text{TiO}_2/\text{CsPbBr}_3$ hybrids for CO_2 photoreduction, *Nat. Commun.* 11 (2020) 4613.
- [42] L.L. Liu, F. Chen, J.H. Wu, J.J. Chen, H.Q. Yu, Synergy of crystallinity modulation and intercalation engineering in carbon nitride for boosted H_2O_2 photosynthesis, *Proc. Natl. Acad. Sci. USA* 120 (2023), e2215305120.
- [43] Z. Dai, F. Qin, H.P. Zhao, J. Ding, Y.L. Liu, R. Chen, Crystal defect engineering of aurivillius Bi_2MoO_6 by Ce doping for increased reactive species production in photocatalysis, *ACS Catal.* 6 (2016) 3180–3192.
- [44] D.Y. Xu, G. Li, Y.L. Dong, Q.W. Wang, J. Zhang, T.S. Yang, S.X. Pang, G.M. Zhang, L.Y. Lv, Y.G. Xia, Z.J. Ren, P.F. Wang, Photocatalytic O_2 activation enhancement and algae inactivation mechanism of $\text{BiO}_{2-x}/\text{Bi}_3\text{NbO}_7$ van der Waals heterojunction, *Appl. Catal. B Environ.* 312 (2022), 121402.
- [45] J. Yang, J.F. Jing, Y.F. Zhu, A full-spectrum porphyrin-fullerene D-A supramolecular photocatalyst with giant Built-in electric field for efficient hydrogen production, *Adv. Mater.* 33 (2021), e2101026.
- [46] J.S. Hu, J. Li, J.F. Cui, W.J. An, L. Liu, Y.H. Liang, W.Q. Cui, Surface oxygen vacancies enriched $\text{FeOOH}/\text{Bi}_2\text{MoO}_6$ photocatalysis-Fenton synergy degradation of organic pollutants, *J. Hazard. Mater.* 384 (2020), 121399.
- [47] P.F. Wang, Y.S. Mao, L. Li, Z.R. Shen, X. Luo, K.F. Wu, P.F. An, H.T. Wang, L.N. Su, Y. Li, S.H. Zhan, Unraveling the interfacial charge migration pathway at the atomic level in a highly efficient Z-scheme photocatalyst, *Angew. Chem. Int. Ed.* 58 (2019) 11329–11334.
- [48] M. Patel, R. Kumar, K. Kishor, T. Mlsna, C.U. Pittman Jr., D. Mohan, Pharmaceuticals of emerging concern in aquatic systems: chemistry, occurrence, effects, and removal methods, *Chem. Rev.* 119 (2019) 3510–3673.
- [49] X. Xiao, R.P. Hu, C. Liu, C.L. Xing, C. Qian, X.X. Zuo, J.M. Nan, L.S. Wang, Facile large-scale synthesis of $\beta\text{-Bi}_2\text{O}_3$ nanospheres as a highly efficient photocatalyst for the degradation of acetaminophen under visible light irradiation, *Appl. Catal. B Environ.* 140–141 (2013) 433–443.
- [50] Z.M. Fang, Y.B. Liu, J.J. Qi, Z.F. Xu, T.Y. Qi, L.D. Wang, Establishing a high-speed electron transfer channel via $\text{CuS}/\text{MIL-Fe}$ heterojunction catalyst for photo-Fenton degradation of acetaminophen, *Appl. Catal. B Environ.* 320 (2023), 121979.